Research article

Highly efficient and 100 % selectivity of CO generation via CO_2 Photoreduction over a novel $CsBr@CuBr_2$ Heterojunction

Jingshan Cui [a], Zhurui Shen [a,b], Gaoqing Cao [a], Xiangxu Zhao [a], Weizun Li [a,*]

[a] *National & Local Joint Engineering Research Center on Biomass Resource Utilization, College of Environmental Science and Engineering, Nankai University, Tianjin, 300350, China*
[b] *School of Materials Science and Engineering, Nankai University, Tianjin, 300350, China*

A B S T R A C T

To address the global challenge posed by excessive carbon dioxide emissions, our research pioneers the transformation of CO_2 into valuable hydrocarbon fuels. Central to this approach is the innovation of photocatalysts, engineered to exhibit exceptional photoresponse characteristics. In this research, the $CsBr@CuBr_2$ photocatalyst was innovatively synthesized through a straightforward and effective one-pot method. The catalyst displayed remarkable efficacy, achieving a CO_2 photoreduction rate of 201.47 µmol g^{-1} within just 4 h. The incorporation of CsBr into $CuBr_2$ effectively captures excited-state electrons, thereby significantly enhancing charge separation efficiency. Utilizing in situ DRIFTS and DFT theoretical analysis, the experiment reveals the complex process of CO_2 photoreduction to CO. The results of this experiment provide breakthrough insights for the systematic design of metal bromide heterostructures, which possess robust CO_2 adsorption/activation potential and notable stability.

1. Introduction

The massive depletion of fossil fuels has not only brought about a non-renewable energy crisis, but has also produced large amounts of carbon dioxide leading to a growing global warming problem [1–3]. Photoreduction of CO_2 into high value-added hydrocarbon fuels, such as CO, CH_4 and CH_3OH, is currently recognized as a sustainable green development strategy that can effectively alleviate current energy and environmental problems [4–6]. However, existing photocatalysts have various defects such as low light absorption efficiency, limited active site, narrow light response range, low reduction efficiency, high carrier recombination rate and poor selectivity [7–10]. In order to achieve more efficient and specialized CO_2 photoreduction, better performing photocatalysts need to be explored [11–13].

Copper-based photocatalysts have been widely used in various photocatalytic systems due to their own advantages, such as low toxicity, abundant earth resources, wide light absorption range, and effective inhibition of charge recombination [14–17]. Among them, CuO, Cu_2O and CuS are the most popular, because of their excellent performance of efficient visible light capture, easy adsorption of CO_2 and directional long-distance electron transfer [18–22]. The copper-based material $CuBr_2$ is often prepared with CsBr to form perovskite and then be used in the photoreduction CO_2 reaction. For example, Dong et al. reported a Cs_2CuBr_4 material, which has a catalytic behavior like SFLPs, effectively changes the CO_2 adsorption mode, improves the CO_2 activation ability, and the CO production rate for 5 h reaches 148.98 µmol g^{-1}, which is 8 times of lead perovskite $CsPbBr_3$ PQDs [23].

The catalytic performance of single-component photocatalysts has different degrees of deficiencies, either in terms of short lifetime of photogenerated carriers or other disadvantages such as narrow light absorption range. Combining two or more catalytic materials to build heterostructures can integrate the advantages of multiple components and effectively improve the catalytic activity. By combining different components, electron redistribution and synergistic effects are generated at the interface. It is also able to generate a new interfacial structure by changing the composition and crystalline phase of the structure, which effectively improves the carrier separation efficiency, broadens the visible light absorption range, and realizes efficient photocatalytic CO_2 reduction [24–28]. Zhou et al. designed 2D/2D Z-type ZnTi-LDH/Cu-FeTCPP MOF heterojunctions, which effectively enhanced the photocatalytic CO_2 reduction efficiency with a CO yield of 37.80 μmol g^{-1}, which was 28 and 26 times higher than that of ZnTi-LDH and CuFe-TCPP MOF photocatalysts, respectively [29].

In this study, $CuBr_2$ was modified with CsBr, and the two formed $CsBr@CuBr_2$ heterojunction. The $CsBr@CuBr_2$ heterojunction has improved the photogenerated carrier separation efficiency and prolonged the lifetime, and the electron mobility was enhanced, which has excellent photocatalytic performance. The efficiency of the CO_2 photo-reduction in 4 h could reach 201.47 μmol g^{-1}, which was better than that of the same type of photocatalytic materials summarized in Table S1[29–38]. In this paper, the mechanistic process of CO_2 photoreduction on $CsBr@CuBr_2$ heterojunction is investigated in detail by in situ infrared characterization and density functional theory calculations. This study provides a simple scheme for the synthesis of metal heterostructures and a new idea for the application of $CsBr@CuBr_2$ photocatalysis.

2. Experimental section

2.1. Chemicals and raw materials

Cs_2CO_3 (99.9 %, Macklin), $CuBr_2$ (99.95 %, Aladdin), MACl (Aladdin), 1,2-Bis (chlorodimethylsilyl) ethane (97 %, Macklin), oleoamine (80–90 %, Macklin), Oleic acid (pharmaceutical grade, Macklin), 1-octadecene (95.0 % (GC), Macklin), toluene (AR, Tianjin Chemical Reagent Supply and Marketing Company).

2.2. Instruments

Ultrasonic Instrument (SCIENTZ SB-5200DT), High Speed Centrifuge (cence TG16-WS), Vacuum Drying Chamber (JINGHONG DZF-6020), Trace Gas Analysis System (PerfectLight Labsolar 6A), Xenon Lamp (PerfectLight PLS-SXE 300+), Vacuum Pump (TINGWEI 2 TW-6G), Circulating Chiller (PerfectLight DC-0506), Air Generator (ZhongHuiPu SPB-3S), Hydrogen Generator (QuanPu QPH-300II), Gas Chromatograph (FULI GC9790II(PLF-01)).

2.3. Material characterizations

XRD was measured on a Rigaku Ultima IV of Japan, with the measuring range of 5–90° and scanning speed of 2° min^{-1}; SEM was characterized on a TESCAN MIRA LMS of Czech Republic; TEM and HRTEM of the material were characterized with a JEOL JEM-F200 of Japan; XPS was carried out by Thermo Scientific ESCALAB 250Xi of America; UV–visible diffuse reflectance spectroscopy was measured on a Shimadzu UV-3600i Plus of Japan; Photoluminescence spectra were measured using an Edinburgh FLS1000 of UK; In situ infrared spectroscopy was carried out in the range of 800–4000 cm^{-1} using an in situ bin spectrometer from Bruker INVENIO-S. Harrick of Germany.

2.4. Synthesis of CsBr@CuBr$_2$

All chemicals were of analytical grade and could be used without further purification in the experiments. 0.6 mmol Cs_2CO_3 and 1.8 mmol $CuBr_2$ precursor powder were added to a 50 mL reagent vial, and then 0.9 mL oleylamine, 3 mL oleic acid, and 30 mL 1-octa-decene were added to the mixture, and sonicated for 30 min using a tip with a power of 300 W. The reaction was completed by centrifugation for 10 min at 9000 rpm. The precipitate was washed twice with toluene and centrifuged at 2000 rpm for 2 min. Then place it in a vacuum oven at 60 °C to dry overnight.

2.5. Photoreduction reaction

The 8 mg photocatalyst was evenly dispersed on the glass fiber filter paper and put into a closed quartz reactor containing 5 mL deionized water together with the gas-solid reaction platform. The system is then vacuumed and filled with high-purity carbon dioxide gas to 80 kPa. Repeat twice to ensure that there are no other gas residues in the system, and turn on the xenon lamp light source for the photoreduction of CO_2. The temperature of the system was ensured to be 278 K throughout the experiment.

3. Results and discussion

The photocatalysts used in the experiments were characterized and analyzed by means of XRD, SEM, TEM, HRTEM, XPS, UV–Vis, PL, EIS, in-situ FTIR and DFT to obtain physical, chemical, and optical properties of the materials.

The crystal structures of the original CsBr, $CuBr_2$ and the synthesized $CsBr@CuBr_2$ were analyzed by XRD test, and the XRD patterns

as shown in Fig. 1. Diffraction peaks of pristine CsBr located at 29.454° and 52.228° can be observed, which correspond to the 110 and 211 planes of the CsBr standard card (JCPDS No. 01–0843), indicating that the original CsBr is a standard CsBr monomer. Compared with the original CsBr, the (110) and (211) peaks of CsBr@CuBr$_2$ do not change except for the decrease in intensity, indicating that CsBr@CuBr$_2$ well retains the main structure of CsBr. Meanwhile, the diffraction peaks of original CuBr$_2$ located at 14.485°, 29.062°, 36.040°, 47.357° and 60.853° are also observed in Fig. 1, corresponding to the CuBr$_2$ standard card (JCPDS No. 17–0771) −101, 002, −221, −213 and −114 planes, in that order. Compared with original CuBr$_2$, the (−221), (−213), and (−114) peaks in CsBr@CuBr$_2$ have slight high-angle shifts, which may be caused by the formation of heterojunction leading to the existence of weak *van der Waals* forces between semiconductors [39]. The XRD pattern analysis shows that CsBr@CuBr$_2$ retains the initial structure of CsBr and CuBr$_2$ and the interaction between CsBr and CuBr$_2$, indicating the successful synthesis of the copper-based heterojunction material CsBr@CuBr$_2$.

The morphology of CsBr@CuBr$_2$ was investigated using SEM, TEM, HRTEM and EDX. As shown in Fig. 2, the single CuBr$_2$ presents a lamellar structure (Fig. 2a) and the single CsBr presents a cell-like shape tightly fitting together (Fig. 2b). When the two were combined to form the heterojunction CsBr@CuBr$_2$, the structure was a main laminar structure with separate small cubes at the tips (Fig. 2c), integrating the structural features of single CuBr$_2$ and single CsBr. Further, the characteristic lattice spacing of 0.514 nm and 0.351 nm corresponding to CsBr (001) and CuBr$_2$ (101) planes is observed in the HRTEM image of CsBr@CuBr$_2$ (Fig. 2d), indicating that a CsBr@CuBr$_2$ heterojunction was formed by contacting the CsBr (001) and CuBr$_2$ (101) faces [40].

Furthermore, the total EDX elemental mapping in Fig. 3a shows the presence of Cs (blue), Cu (red) and Br (green) elements of CsBr@CuBr$_2$. Fig. 3b–c correspondingly show the distribution characteristics of Cs, Cu and Br elements of CsBr@CuBr$_2$, and it can be seen that all the three elements show a uniform distribution. These results strongly demonstrate the successful synthesis of CsBr@CuBr$_2$.

In order to further understand the elemental composition and chemical state of CsBr@CuBr$_2$, X-Ray Photoelectron Spectroscopy (XPS) was carried out, and the resulting total spectrum is shown in Fig. 4a. The characteristic peaks of Cu, Cs, Br and C elements can be observed in Fig. 4a, indicating that the element composition of CsBr@CuBr$_2$ is Cu, Cs and Br, which is consistent with the expectation.

The Cs 3d, Cu 2p and Br 3d binding energy signals of CsBr@CuBr$_2$, CsBr and CuBr$_2$ were superimposed, compared and analyzed. Fig. 4b shows the high-resolution XPS spectrum of Cs 3d. Two peaks of 738.5 and 724.6 eV in CsBr@CuBr$_2$ can be observed, which correspond to the binding energies of Cs 3d$_{2/3}$ and Cs 3d$_{5/2}$, respectively. In the XPS spectrum of Cu 2p (Fig. 4c), the binding energies of Cu 2p$_{1/2}$ of CsBr@CuBr$_2$ is shown as two peaks of 951.8 eV and 962.5 eV, and the binding energy of Cu 2p$_{3/2}$ exhibited two peaks at 931.9eV and 943.0 eV. The two peaks of 69.7 and 68.7 eV in the Br 3d spectrum (Fig. 4d) are in turn attributed to the Br-states of the binding energies of Br 3d$_{1/2}$ and Br 3d$_{5/2}$ [41,42]. However, the peaks of CsBr@CuBr$_2$ are slightly shifted compared to the single-component CsBr and CuBr$_2$.

Usually, the binding energy shift in composites can be explained by the strong interaction between different components [43]. Unlike the 0.62 eV shift for Br 3d, the binding energy shifts for Cs 3d and Cu 2p are 1.70 and 1.36 eV, respectively. The larger shifts for Cs and Cu indicate that the Cs–Cu interaction is stronger than the Br–Cs and Br–Cu interactions. The XPS of the low energy segment of CsBr and CuBr$_2$ is shown in Fig. S1. CsBr and CuBr$_2$ were measured to be 0.50 eV and −0.72 eV, respectively, by the tangent method.

Through experiments, it was found that the synthesis of CsBr@CuBr$_2$ had the best photoreduction CO$_2$ performance when the mass of MACl accounted for 20 % and the mass concentration of 1,2-Bis (chlorodimethylsilyl) ethane was 1.0 mg/mL (Fig. 5a and b), and the synthesis conditions were determined as CsBr@CuBr$_2$. Next, the efficiency of photocatalytic reduction of CO$_2$ by CsBr, CuBr$_2$ and CsBr@CuBr$_2$ was specifically tested. The only photoreduction CO$_2$ product under the action of the three catalysts is CO. As shown in Fig. 5c, the yields of CO for both CsBr and CuBr$_2$ increased gradually with the extension of the light time, the yields of CO reached
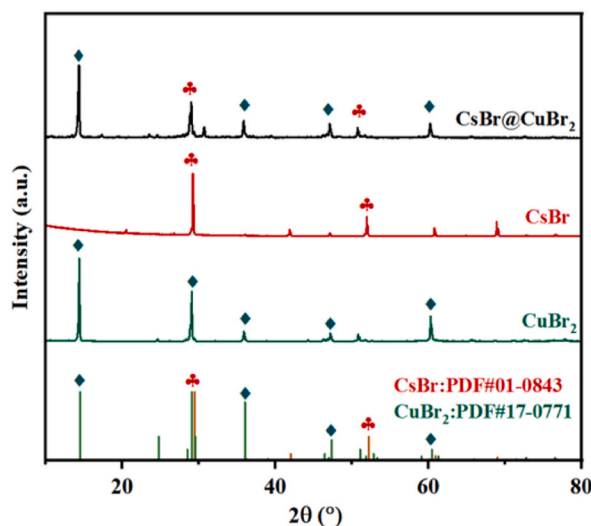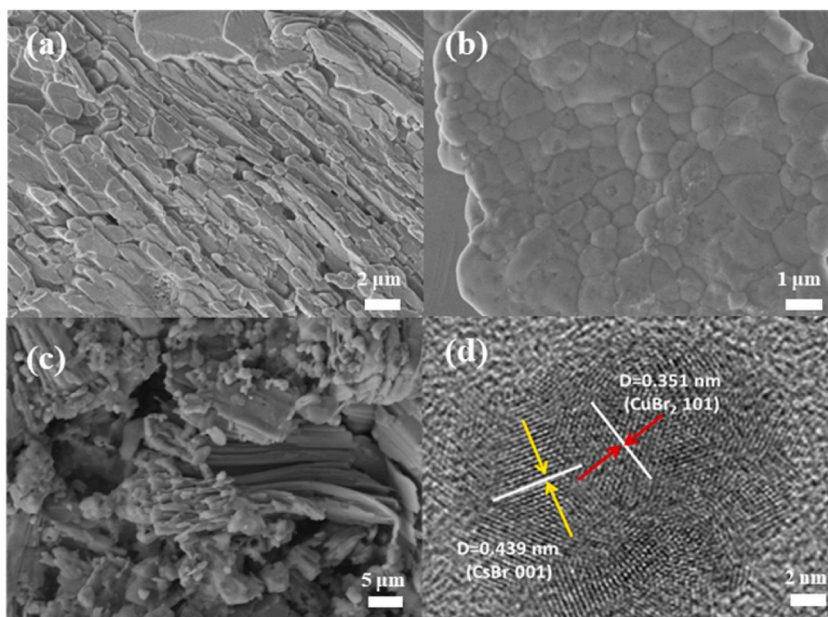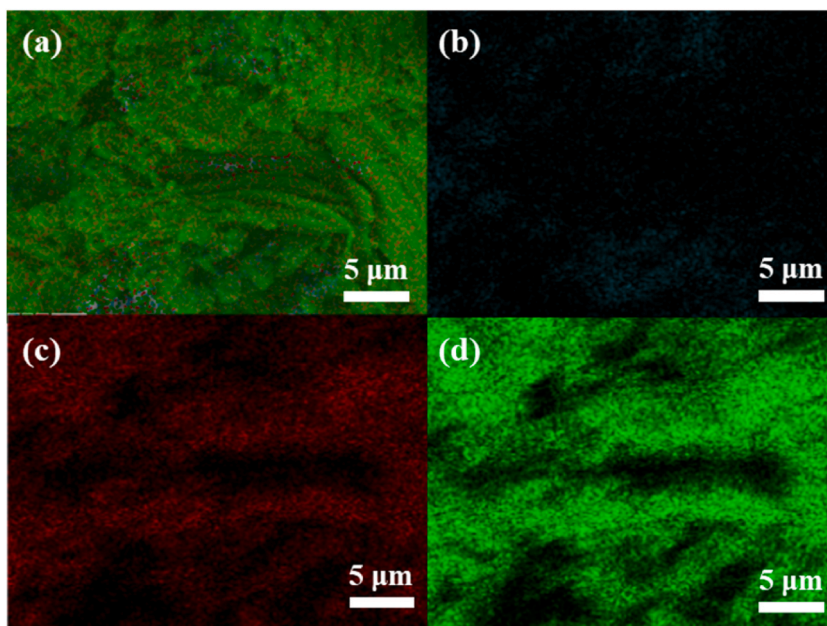
Fig. 1. XRD patterns of CsBr, CuBr$_2$, and CsBr@CuBr$_2$.

Fig. 2. SEM of CuBr$_2$ (a), CsBr (b), and CsBr@CuBr$_2$ (c). (d) HRTEM of CsBr@CuBr$_2$.

Fig. 3. EDX elemental mappings of Total element (a), Cs (b), Cu (c) and Br (d) of CsBr@CuBr$_2$.

21.42 μmol g^{-1} and 44.17 μmol g^{-1} respectively, after 4 h. However, when CsBr@CuBr$_2$ was formed by the one-pot method, the yield of CO increased to 201.47 μmol g^{-1}. Compared with the original material, the yield was more than six times. After seven cycles, CsBr@CuBr$_2$ still achieves more than 70 % initial efficiency (Fig. 5d).

The optical properties of CsBr@CuBr$_2$, CuBr$_2$ and CsBr were analyzed by UV–vis diffuse reflectance spectroscopy. In contrast to the absorption of CuBr$_2$ and CsBr, CsBr@CuBr$_2$ exhibits significant and broad absorption in both UV and visible ranges (Fig. 6a). The enhancement of the light-absorbing region may be related to the introduction of Cs ions and the electron transfer after assembly with reduced clusters [44]. Subsequently, the optical bandgap energies of CuBr$_2$, and CsBr were further measured by Tauc plots, which were 2.02 and 4.64 eV, respectively (Fig. 6b).

The carrier separation/migration in CsBr@CuBr$_2$ and CuBr$_2$ was further explored using PL experiment. Compared with CuBr$_2$,
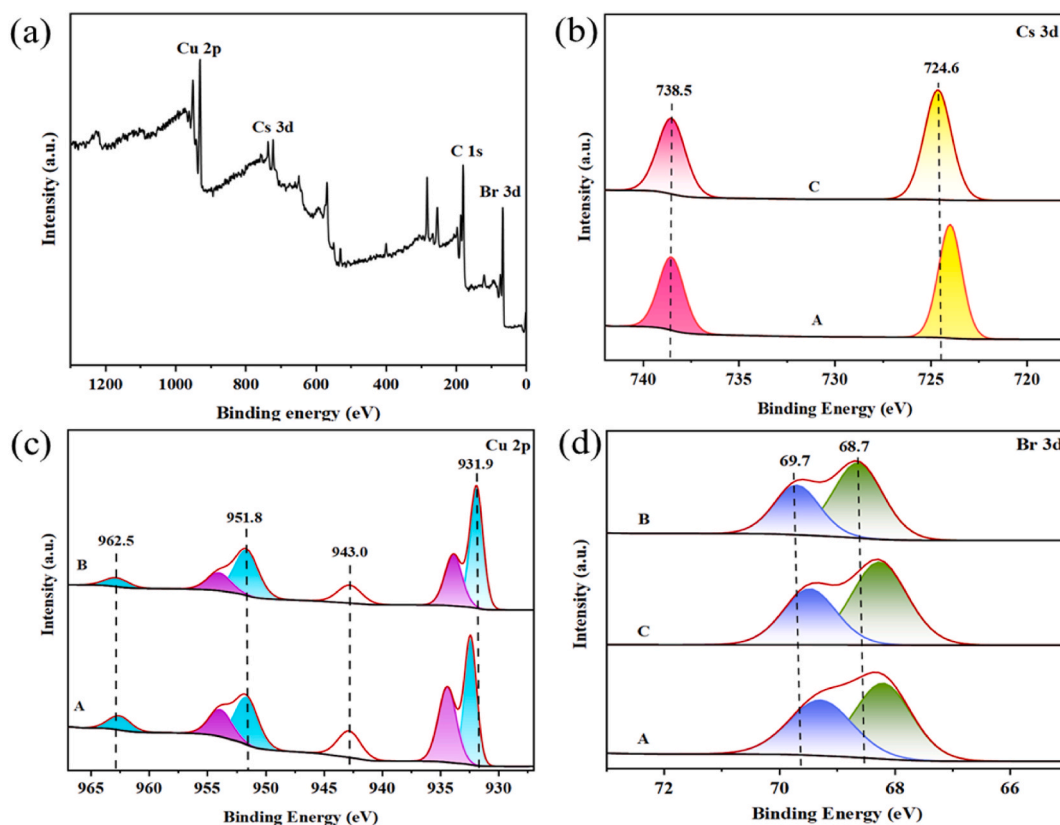
Fig. 4. (a) XPS survey spectra of CsBr@CuBr$_2$. XPS spectra of Cs 3d (b), Cu 2p (c) and Br 3d (d) of CsBr@CuBr$_2$(A), CuBr$_2$(B) and CsBr(C).

which exhibited an extremely high steady-state PL intensity at 440 nm excitation wavelength (Fig. 7a), the PL intensity of CsBr@CuBr$_2$ at 225 nm excitation wavelength was significantly reduced, which indicated that CsBr@CuBr$_2$ effectively blocked the recombination of photogenerated electron/hole pairs. It suggests that the addition of CsBr improves the charge separation ability in the photocatalytic CO$_2$ reduction process, reduces the complexation rate between e$^-$/H$^+$, and enhances the inhibition of photogenerated carrier complexation [45].

The charge transport behaviors of CsBr@CuBr$_2$ and CuBr$_2$ were further investigated by EIS (Fig. 7b). CsBr@CuBr$_2$ presents a smaller arc diameter on the EIS curves than that of CuBr$_2$. Further simulation results show that the charge-transfer resistances of CsBr@CuBr$_2$ and CuBr$_2$ are 284.1 Ω and 345.1 Ω, respectively. It shows that CsBr@CuBr$_2$ exhibits a lower charge-transfer resistance and a higher charge-transfer efficiency than that of CuBr$_2$, which leads to a photoexcited excellent separation efficiency of electrons for e$^-$/h$^+$, in agreement with the results obtained from PL experiments [30] The excellent photocurrent signal of CsBr@CuBr$_2$ on the transient photocurrent curve also indicates its excellent charge separation efficiency (Fig. S2). The excellent charge transport properties of CsBr@CuBr$_2$ may be attributed to the presence of abundant reaction sites.

In order to gain insight into the catalytic pathway of the CO$_2$ photoreduction reaction, the intermediates in the photocatalytic reduction of CO$_2$ by CsBr@CuBr$_2$ were dynamically identified and monitored by in situ infrared tests. In Fig. 8a and b, peaks at 1260 and 1455 cm^{-1} can be observed, which are attributed to carbonate species (CO$_3^{2-}$) [46]; peaks at 1218 and 1422 cm^{-1} are characteristic of HCO$_3^-$ species, which are formed by the carbonate species formed by protonation [40]; peaks of CO$_2$* radicals were detected at 1596 cm^{-1}, which is a key indicator of CO$_2$ binding to electrons [44,47]. In addition, *COOH (1476 and 1520 cm^{-1}) and CO* (1710 and 1725 cm^{-1}) peaks, providing direct evidence for the multi-step hydrogenation of CO$_2$ to CO [40,48–51]. The main characteristic peaks in the figure maintain a stable increasing trend, indicating that CsBr@CuBr$_2$ has good activity and stability in the photocatalytic reduction of CO$_2$. As shown in Fig. 8c and d, the intermediate product of CO$_2$ reduction by CuBr$_2$ to CO is consistent with that shown in CsBr@CuBr$_2$, but the peak intensities are lower, indicating that its photoreduction performance is weaker than that of CsBr@CuBr$_2$. Based on the results of in situ FTIR test analysis, the photocatalytic CO$_2$ reduction pathway on CsBr@CuBr$_2$ and CuBr$_2$ is proposed (Equations. 1-8).

$$CO_2 + H_2O \rightarrow H_2CO_3 \tag{1}$$

$$H_2CO_3 \rightarrow H^+ + HCO_3^- \tag{2}$$
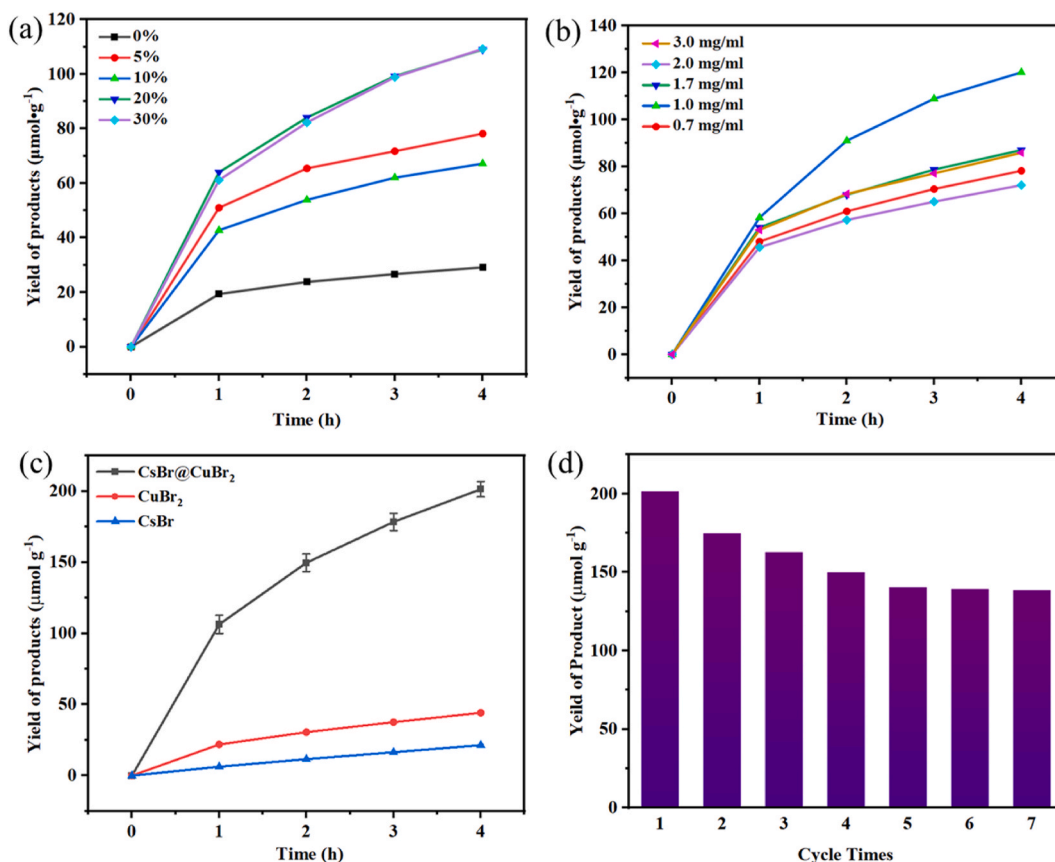
Fig. 5. (a) CO yields of different MACL mass ratios. (b) CO yields of different 1,2-Bis (chlorodimethylsilyl) ethane concentrations. (c) CO yields of CsBr@CuBr$_2$, CuBr$_2$ and CsBr. (d) Cycle stability test of CsBr@CuBr$_2$.
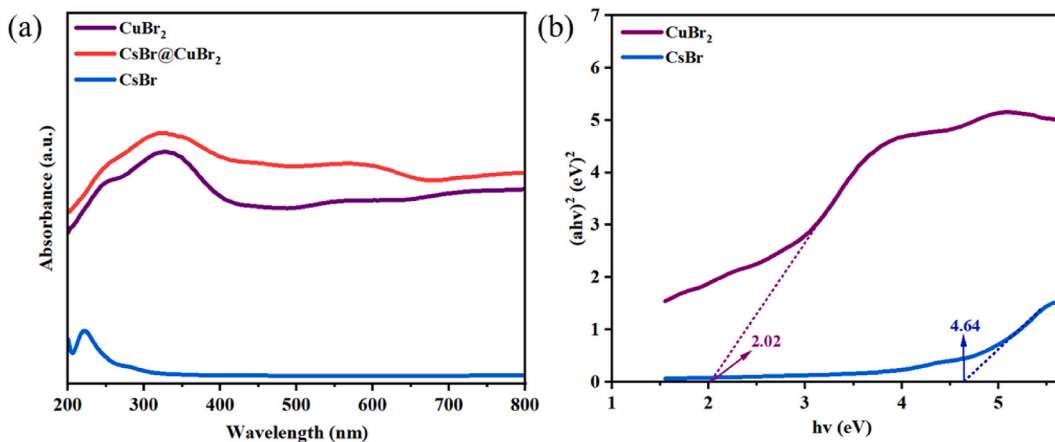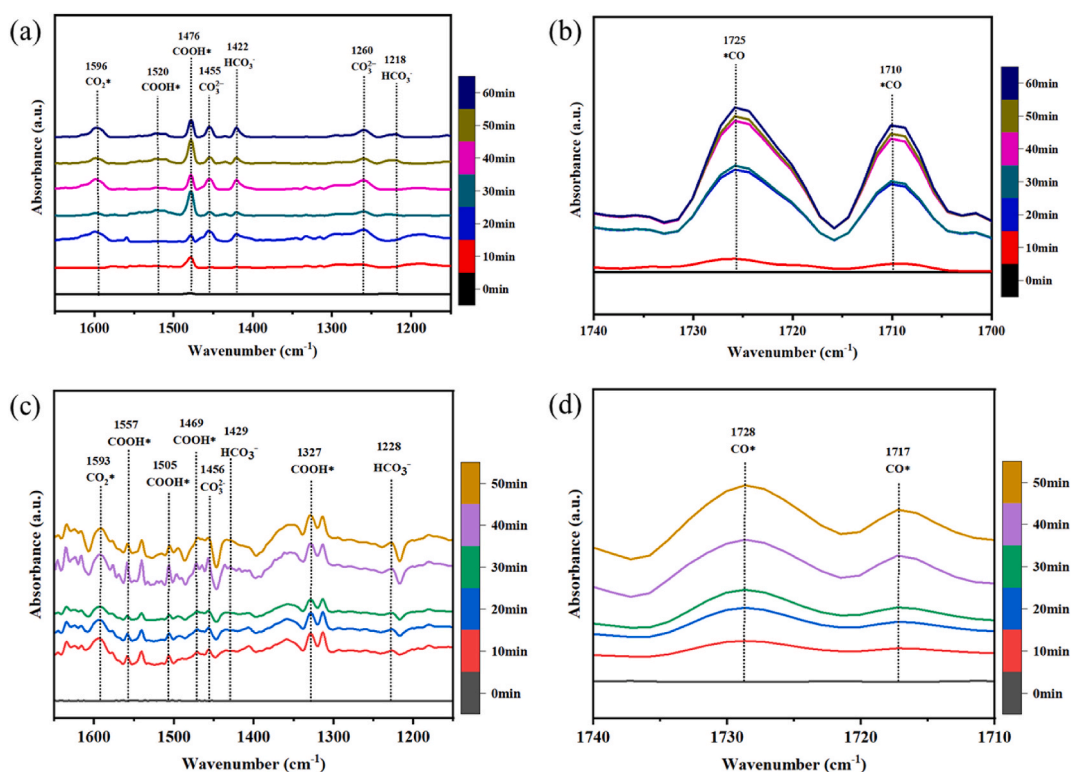

Fig. 6. (a)UV–vis diffuse reflectance spectra of CuBr$_2$, CsBr and CsBr@CuBr$_2$. (b) Band gap energy (Eg) analysis for CuBr$_2$, CsBr and CsBr@CuBr$_2$.

$$HCO_3^- \rightarrow H^+ + CO_3^{2-} \tag{3}$$

$$CsBr@CuBr_2 \xrightarrow{h\nu} h^+ + e^- \tag{4}$$

$$CO_2 + * \rightarrow CO_2^* \tag{5}$$
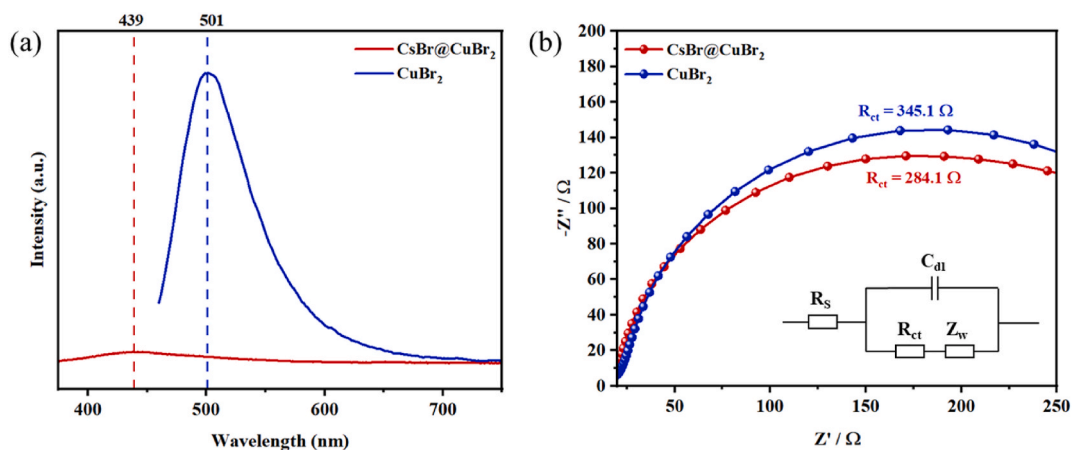
Fig. 7. (a) PL spectra of CsBr@CuBr$_2$ and CuBr$_2$. (b) Electrochemical impedance spectra (EIS) of CsBr@CuBr$_2$ and CuBr$_2$.

Fig. 8. In situ FTIR spectroscopy characterization. (a,b) In-situ FTIR spectra of CsBr@CuBr$_2$ in the presence of CO$_2$ and H$_2$O vapor within 60 min illumination. (c,d) In-situ FTIR spectra of CuBr$_2$ in the presence of CO$_2$ and H$_2$O vapor within 50 min illumination.

$$CO_2^* + H^+ + e^- \rightarrow COOH^* \tag{6}$$

$$COOH^* + H^+ + e^- \rightarrow CO^* \tag{7}$$

$$CO^* \rightarrow CO + * \tag{8}$$

As shown in Fig. 9a and b, DFT calculations yielded the CO$_2$ reduction reaction pathway as the excitation of CO$_2$ to *CO$_2$, which is then converted to *COOH, then generates *CO, and finally the desorption of *CO to obtain CO, which is consistent with the in situ FTIR results. The Gibbs free energy of CO$_2$ photoreduction reaction on CuBr$_2$ and CsBr@CuBr$_2$ heterojunctions was investigated to further reveal the reason for the improved performance of photocatalytic reduction of CO$_2$ by CsBr@CuBr$_2$ heterojunctions. The free energies
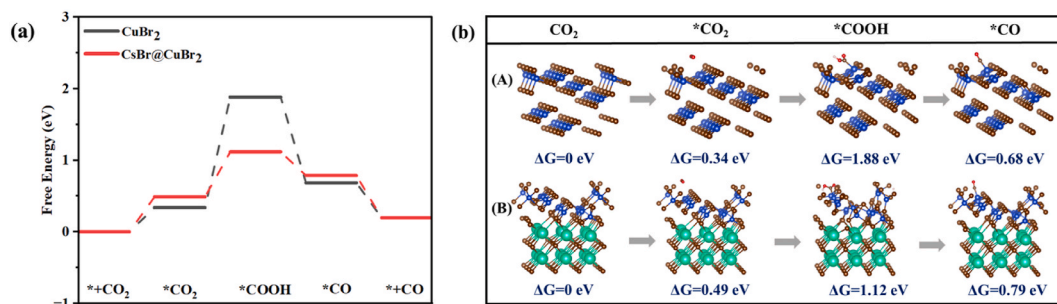
Fig. 9. (a) Gibbs free energy diagrams for intermediates on $CuBr_2$ and $CsBr@CuBr_2$. (b) Structure models of Gibbs free energy calculations of CO_2 photoreduction pathways over $CuBr_2$(A) and $CsBr@CuBr_2$(B).

of CO_2*, $COOH*$ and $CO*$ on $CuBr_2$ are 0.34, 1.88 and 0.68 eV, respectively, and the free energies of the three substances on $CsBr@CuBr_2$ heterojunction are 0.49, 1.12 and 0.79 eV, respectively. Compared with $CuBr_2$, the barrier energies for $COOH*$ formation from $CsBr@CuBr_2$ are significantly lower, which is favorable for the dynamic charge migration between $CuBr_2$ and $CsBr$, and easier $COOH*$ formation. From a thermodynamic point of view, the step of formation of $COOH*$ from $*CO_2$ is the rate-determining step of the CO_2 photoreduction process [50,52] , thus $CsBr@CuBr_2$ is more favorable for CO_2 reduction.

VB and Eg of $CsBr$ and $CuBr_2$ as mentioned above. The CB of $CsBr$ and $CuBr_2$ were calculated to be −4.14 eV and −2.74 eV respectively, based on ECB = EVB- Eg. The energy band structure and photocatalytic mechanism of $CsBr@CuBr_2$ were then deduced as shown in Fig. 10. The $CsBr@CuBr_2$ interface forms a type I heterojunction with $CuBr_2$ as electron acceptor. Due to the Cs–Cu interface bond channel between $CsBr$ and $CuBr_2$, these hot electrons from excited $CsBr$ easily migrate to $CuBr_2$, resulting in efficient charge separation in $CsBr@CuBr_2$. Electrons participate in the reduction of CO_2 molecules to CO, and holes participate in the oxidation of H_2O to O_2, ensuring the efficient photocatalytic reaction.

4. Conclusion

In summary, in this study, metal bromide heterojunction $CsBr@CuBr_2$ was synthesized by a simple one-pot method, which was concluded to be a single-product and highly efficient catalyst for photo-reduction of CO_2 by experimental and related photochemical characterization. Compared to the photoreduction CO_2 4 h efficiency of $CsBr$ 21.42 μmol g^{-1} and $CuBr_2$ 44.17 μmol g^{-1}, $CsBr@CuBr_2$ could reach 201.47 μmol g^{-1}. The photoreduction CO_2 efficiency of $CsBr@CuBr_2$ was increased by 9.4 times compared with the $CsBr$ and 4.5 times compared with the $CuBr_2$, which had more excellent photocatalytic performance. XRD, SEM, TEM, and HRTEM characterizations showed the successful synthesis of $CsBr@CuBr_2$, and PL, UV–Vis diffuse reflectance, and EIS showed that the resulting $CsBr@CuBr_2$ heterojunctions possessed excellent photon trapping, sufficient surface redox potential, and fast photoexcited charge separation properties when $CsBr$ was introduced into $CuBr_2$. Density Functional Theory (DFT) calculations show that $CsBr@CuBr_2$ effectively reduces the reaction energy barrier. These demonstrate the favorable aspects of $CsBr@CuBr_2$ for CO_2 photoreduction. In addition, this study provides a new strategy and direction for the rapid synthesis of metal heterojunction materials for efficient photoreduction of CO_2.
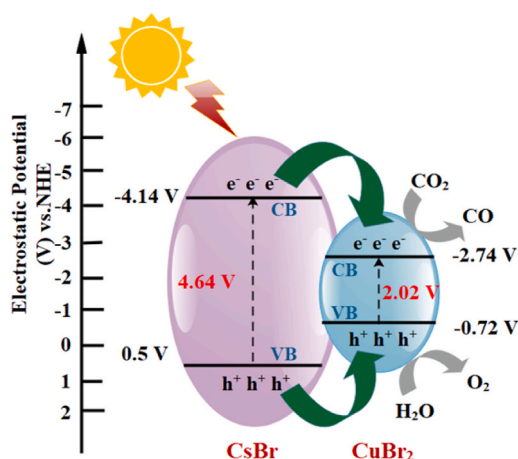
Fig. 10. Proposed mechanism on photocatalytic reduction of CO_2 into CO on the $CsBr@CuBr_2$.

Data availability statement

Data is not stored in a publicly available repository. Data will be made available on request.

Ethics declarations

Review and/or approval by an ethics committee was not needed for this study because there were no ethical issues involved in this study.

CRediT authorship contribution statement

Jingshan Cui: Writing – original draft, Formal analysis, Data curation. **Zhurui Shen:** Writing – review & editing, Methodology, Conceptualization. **Gaoqing Cao:** Validation. **Xiangxu Zhao:** Investigation. **Weizun Li:** Writing – review & editing, Supervision.

Declaration of competing interest

The authors declare that they have no known competing financial interests or personal relationships that could have appeared to influence the work reported in this paper.

Acknowledgements

Appendix A. Supplementary data

Supplementary data to this article can be found online at https://doi.org/10.1016/j.heliyon.2024.e33653.

References

[1] M. Hook, X. Tang, Depletion of fossil fuels and anthropogenic climate change-A review, Energy Policy 52 (2013) 797–809, https://doi.org/10.1016/j.enpol.2012.10.046.

[2] S.J. Davis, K. Caldeira, H.D. Matthews, Future CO_2 emissions and climate change from existing energy infrastructure, Science 329 (2010) 1330–1333, https://doi.org/10.1126/science.1188566.

[3] K. Yang, et al., Recent advances in CdS-based photocatalysts for CO_2 photocatalytic conversion, Chem. Eng. J. 418 (2021), https://doi.org/10.1016/j.cej.2021.129344.

[4] A.D. Handoko, K. Li, J. Tang, Recent progress in artificial photosynthesis: CO_2 photoreduction to valuable chemicals in a heterogeneous system, Curr. Opin. Chem. Eng. 2 (2013) 200–206, https://doi.org/10.1016/j.coche.2012.12.003.

[5] T.A. Saleh, Organic-inorganic hybrid nanocomposites for the photoreduction of CO_2: environment and energy technologies, Bull. Mater. Sci. 45 (2022), https://doi.org/10.1007/s12034-022-02807-0.

[6] B. Han, X. Ou, Z. Deng, Y. Song, C. Tian, H. Deng, Y.-J. Xu, Z. Lin, Nickel metal-organic framework monolayers for photoreduction of diluted CO_2: metal-node-dependent activity and selectivity, Angew. Chem. Int. Ed. 57 (2018) 16811–16815, https://doi.org/10.1002/ange.201811545.

[7] Y.Y. Lee, H.S. Jung, Y.T. Kang, A review: effect of nanostructures on photocatalytic CO_2 conversion over metal oxides and compound semiconductors, J. CO_2 Util. 20 (2017) 163–177, https://doi.org/10.1016/j.jcou.2017.05.019.

[8] Y. Liu, C. Tang, M. Cheng, M. Chen, S. Chen, L. Lei, Y. Chen, H. Yi, Y. Fu, L. Li, Polyoxometalate@Metal-Organic framework composites as effective photocatalysts, ACS Catal. 11 (2021) 13374–13396.

[9] C. Xia, et al., The emerging covalent organic frameworks (COFs) for solar-driven fuels production, Coord. Chem. Rev. 446 (2021), https://doi.org/10.1021/acsc.atal.1c03866.

[10] E. Gong, S. Ali, C.B. Hiragond, H.S. Kim, N.S. Powar, D. Kim, H. Kim, S.-I. In, Solar fuels: research and development strategies to accelerate photocatalytic CO_2 conversion into hydrocarbon fuels, Energy Environ. Sci. 15 (2022) 880–937, https://doi.org/10.1039/D1EE02714J.

[11] J. Sheng, Y. He, J. Li, C. Yuan, H. Huang, S. Wang, Y. Sun, Z. Wang, F. Dong, Identification of halogen-associated active sites on bismuth-based perovskite quantum dots for efficient and selective CO_2-to-CO photoreduction, ACS Nano 14 (2020) 13103–13114, https://doi.org/10.1021/acsnano.0c04659.

[12] S. Shyamal, S.K. Dutta, T. Das, S. Sen, S. Chakraborty, N. Pradhan, Facets and defects in perovskite nanocrystals for photocatalytic CO_2 reduction, J. Phys. Chem. Lett. 11 (2020) 3608–3614, https://doi.org/10.1021/acs.jpclett.0c01088.

[13] M. Ou, W. Tu, S. Yin, W. Xing, S. Wan, H. Wang, S. Wan, Q. Zhong, R. Xu, Amino-assisted anchoring of $CsPbBr_3$ perovskite quantum dots on porous g-C_3N_4 for enhanced photocatalytic CO_2 reduction, Angew. Chem. Int. Ed. 57 (2018) 13570–13574, https://doi.org/10.1002/anie.201808930.

[14] S. Sun, X. Zhang, Q. Yang, S. Liang, X. Zhang, Z. Yang, Cuprous oxide (Cu_2O) crystals with tailored architectures: a comprehensive review on synthesis, fundamental properties, functional modifications and applications, Prog. Mater. Sci. 96 (2018) 111–173, https://doi.org/10.1016/j.pmatsci.2018.03.006.

[15] W. Luo, et al., ZnS:Cu powders with strong visible-light photocatalysis and pyro-catalysis for room-temperature dye decomposition, Ceram. Int. 46 (2020) 12096–12101, https://doi.org/10.1016/j.ceramint.2020.01.253.

[16] F. Zhang, H.-Q. Zhuang, W. Zhang, J. Yin, F.-H. Cao, Y.-X. Pan, Noble-metal-free CuS/CdS photocatalyst for efficient visible-light-driven photocatalytic H_2 production from water, Catal. Today. 330 (2019) 203–208, 10.101.6/j.cattod.2018.03.060.

[17] T. Mandal, N. Katta, H. Paps, O. Reiser, Merging Cu(I) and Cu(II) photocatalysis: development of a versatile oxohalogenation protocol for the sequential Cu(II)/Cu(I)-Catalyzed oxoallylation of vinylarenes, ACS org, Inorg. Au. 3 (2023) 171–176, https://doi.org/10.1021/acsorginorgau.3c00011.

[18] J.-Y. Li, L. Yuan, S.-H. Li, Z.-R. Tang, Y.-J. Xu, One-dimensional copper-based heterostructures toward photo-driven reduction of CO_2 to sustainable fuels and feedstocks, J. Mater. Chem. A 7 (2019) 8676–8689, https://doi.org/10.1039/C8TA12427B.

[19] H. Xie, J. Wang, K. Ithisuphalap, G. Wu, Q. Li, Recent advances in Cu-based nanocomposite photocatalysts for CO_2 conversion to solar fuels, J. Energy Chem. 26 (2017) 1039–1049, https://doi.org/10.1016/j.jechem.2017.10.025.

[20] Y.-H. Zhang, M.-M. Liu, J.-L. Chen, S.-M. Fang, P.-P. Zhou, Recent advances in Cu₂O-based composites for photocatalysis: a review, Dalton Trans. 50 (2021) 4091–4111, https://doi.org/10.1039/D0DT04434B.

[21] W. Wang, L. Wang, W. Su, Y. Xing, Photocatalytic CO₂ reduction over copper-based materials: a review, J. CO₂ Util. 61 (2022), https://doi.org/10.1016/j.jcou.2.022.102056.

[22] S. Ali, A. Razzaq, H. Kim, S.-I. In, Activity, selectivity, and stability of earth-abundant CuO/Cu₂O/Cu⁰-based photocatalysts toward CO₂ reduction, Chem. Eng. J. 429 (2022), https://doi.org/10.1016/j.cej.2021.131579.

[23] J. Sheng, Y. He, M. Huang, C. Yuan, S. Wang, F. Dong, Frustrated Lewis pair sites boosting CO₂ photoreduction on Cs₂CuBr₄ perovskite quantum dots, ACS Catal. 12 (2022) 2915–2926, https://doi.org/10.1021/acscatal.2c00037.

[24] Y. Li, M. Zhou, B. Cheng, Y. Shao, Recent advances in g-C₃N₄-based heterojunction photocatalysts, J. Mater. Sci. Technol. 56 (2020) 1–17, https://doi.org/10.1016/j.jmst.2020.04.028.

[25] N. Li, X. Chen, J. Wang, X. Liang, L. Ma, X. Jing, D.-L. Chen, Z. Li, ZnSe nanorods-CsSnCl₃ perovskite heterojunction composite for photocatalytic CO₂ reduction, ACS Nano 16 (2022) 3332–3340, https://doi.org/10.1021/acsnano.1c11442.

[26] X. Wang, Y. Wang, M. Gao, J. Shen, X. Pu, Z. Zhang, H. Lin, X. Wang, BiVO₄/Bi₄Ti₃O₁₂ heterojunction enabling efficient photocatalytic reduction of CO₂ with H₂O to CH₃OH and CO, Appl. Catal. B 270 (2020), https://doi.org/10.1016/j.apcatb.2020.118876.

[27] G. Zhang, Z. Wang, J. Wu, Construction of a Z-scheme heterojunction for high-efficiency visible-light-driven photocatalytic CO₂ reduction, Nanoscale 13 (2021) 4359–4389, https://doi.org/10.1039/D0NR08442E.

[28] Z. Zhang, L. Li, Y. Jiang, J. Xu, Step-scheme photocatalyst of CsPbBr₃ quantum dots/BiOBr nanosheets for efficient CO₂ photoreduction, Inorg. Chem. 61 (2022) 3351–3360, https://doi.org/10.1021/acs.inorgchem.2c00012.

[29] C. Zhou, Y. Yang, G. Wu, M. Mu, X. Yin, 2D Cu-FeTCPP MOF assembled on ZnTi-LDH to construct 2D/2D direct Z-scheme heterojunction for enhanced photocatalytic CO₂ reduction, Sol. Energy 253 (2023) 480–490, https://doi.org/10.1016/j.solener.2023.02.058.

[30] Y. Li, Q. Yin, Y. Zeng, Z. Liu, Hollow spherical biomass derived-carbon dotted with SnS₂/g-C₃N₄ Z-scheme heterojunction for efficient CO₂ photoreduction into CO, Chem. Eng. J. 438 (2022), https://doi.org/10.1016/j.cej.2022.135652.

[31] Z. Jiang, et al., Living atomically dispersed Cu ultrathin TiO₂ nanosheet CO₂ reduction photocatalyst, Adv. Sci. 6 (2019) 1900289, https://doi.org/10.1002/advs.201900289.

[32] S. Kumar, M. Regue, M.A. Isaacs, E. Freeman, S. Eslava, All-Inorganic CsPbBr₃ nanocrystals: gram-scale mechanochemical synthesis and selective photocatalytic CO₂ reduction to methane, ACS Appl. Energy Mater. 3 (2020) 4509–4522, https://doi.org/10.1021/acsaem.0c00195.

[33] X. Wang, J. He, J. Li, G. Lu, F. Dong, T. Majima, M. Zhu, Immobilizing perovskite CsPbBr₃ nanocrystals on Black phosphorus nanosheets for boosting charge separation and photocatalytic CO₂ reduction, Appl. Catal. B Environ. 277 (2020) 119230, https://doi.org/10.1016/j.apcatb.2020.119230. Applied Catalysis B-Environmental, 2020, 277.

[34] Y.W. Teh, Y.W. Goh, X.Y. Kong, B.-J. Ng, S.-T. Yong, S.-P. Chai, Fabrication of Bi₂WO₆/Cu/WO₃ all-solid-state Z-scheme composite photocatalyst to improve CO₂ photoreduction under visible light irradiation, ChemCatChem 11 (2019) 6431–6438, https://doi.org/10.1002/cctc.201901653.

[35] X. Zhao, L. Sun, X. Jin, M. Xu, S. Yin, J. Li, X. Li, D. Shen, Y. Yan, P. Huo, Cu media constructed Z-scheme heterojunction of UiO-66-NH₂/Cu₂O/Cu for enhanced photocatalytic induction of CO₂, Appl. Surf. Sci. 545 (2021) 148967, https://doi.org/10.1016/j.apsusc.2021.148967.

[36] L. Li, Z. Zhang, In-situ fabrication of Cu doped dual-phase CsPbBr₃-Cs₄PbBr₆ inorganic perovskite nanocomposites for efficient and selective photocatalytic CO₂ reduction, Chem. Eng. J. 434 (2022) 134811, https://doi.org/10.1016/j.cej.2022.134811.

[37] L. Wu, S. Zheng, H. Lin, S. Zhou, A.M. Idris, J. Wang, S. Li, Z. Li, In-situ assembling 0D/2D Z-scheme heterojunction of Lead-free Cs₂AgBiBr₆/Bi₂WO₆ for enhanced photocatalytic CO₂ reduction, J. Colloid Interface Sci. 629 (2023) 233–242, https://doi.org/10.1016/j.jcis.2022.08.152.

[38] Z. Zhang, D. Li, Z. Dong, Y. Jiang, X. Li, Y. Chu, J. Xu, Lead-Free Cs₂AgBiBr₆ Nanocrystals Confined in MCM-48 Mesoporous Molecular Sieve for Efficient Photocatalytic CO₂ Reduction, Solar Rrl 7 (2023) 2300038, 10.10.02/solr.202300038.

[39] Y. Li, Q. Yin, Y. Zeng, Z. Liu, Hollow spherical biomass derived-carbon dotted with SnS₂/g-C₃N₄ Z-scheme heterojunction for efficient CO₂ photoreduction into CO, Chem. Eng. J. 438 (2022) 135652, https://doi.org/10.1016/j.cej.2022.135652.

[40] Z. Zhang, D. Li, H. Hu, Y. Chu, J. Xu, In situ growth of lead-free Cs₂CuBr₄ perovskite quantum dots in KIT-6 mesoporous molecular sieve for CO₂ adsorption, activation, and reduction, Inorg. Chem. 62 (2023) 9240–9248, https://doi.org/10.1021/acs.inorgchem.3c01189.

[41] Y. Zhiyong, D. Bahnemann, R. Dillert, S. Lin, L. Liqin, Photocatalytic degradation of azo dyes by BiOX (X = Cl, Br), J. Mol. Catal. Chem. 365 (2012) 1–7, https://doi.org/10.1016/j.molcata.2012.07.001.

[42] Z. Dong, Z. Zhang, Y. Jiang, Y. Chu, J. Xu, Embedding CsPbBr₃ perovskite quantum dots into mesoporous TiO₂ beads as an S-scheme heterojunction for CO₂ photoreduction, Chem. Eng. J. 433 (2022), https://doi.org/10.1016/j.cej.2021.133762.

[43] X. Wang, J. He, J. Li, G. Lu, F. Dong, T. Majima, M. Zhu, Immobilizing perovskite CsPbBr₃ nanocrystals on Black phosphorus nanosheets for boosting charge separation and photocatalytic CO₂ reduction, Appl. Catal. B Environ. 277 (2020), https://doi.org/10.1016/j.apcatb.2020.119230.

[44] J. Wang, H. Xu, Q. Wang, J. Zhou, X. Xiang, S. Li, H. Mei, Y. Xu, Self-assembly of mixed valence polyoxovanadate-based metal-organic frameworks for enhanced CO₂ photoreduction, Chem. Eng. J. 474 (2023), 10.10.1.6./j.cej.2023.145662.

[45] L. Huang, et al., Designing multi-layered MOF-on-MOF-transformed core double-shell FeSₓ@ZnS@CoSₓ heterojunction for enhanced CO₂ photoreduction with water vapor, Chem. Eng. J. 474 (2023), https://doi.org/10.1016/j.cej.2023.1.45740.

[46] B. Zhou, et al., Synergistic effects of heterointerface and surface Br vacancies in ultrathin 2D/2D H₂WO₄/Cs₂AgBiBr₆ for efficient CO₂ photoreduction to CH₄, Chem. Eng. J. 468 (2023), https://doi.org/10.1016/j.cej.2023.143754.

[47] H. Yang, H. Hou, M. Yang, Z. Zhu, H. Fu, D. Zhang, Y. Luo, W. Yang, Engineering the S-scheme heterojunction between NiO microrods and MgAl-LDH nanoplates for efficient and selective photoreduction of CO₂ to CH₄, Chem. Eng. J. 474 (2023), https://doi.org/10.1016/j.cej.2023.145813.

[48] Z. Wang, B. Cheng, L. Zhang, J. Yu, H. Tan, Single metal–organic cage decorated with an Ir(III) complex for CO2 photoreduction, Sol. RRL 6 (2022), https://doi.org/10.1021/acscatal.1c01974.

[49] H. Zhang, J. Ma, S. Wang, J. Ji, Z. Zeng, Z. Shen, Y. Du, C.-H. Yan, Novel cerium-based sulfide nano-photocatalyst for highly efficient CO₂ reduction, Small 18 (2022), https://doi.org/10.1002/smll.202201332.

[50] Y. Li, Q. Yin, Y. Zeng, Z. Liu, Hollow spherical biomass derived-carbon dotted with SnS₂/g-C₃N₄ Z-scheme heterojunction for efficient CO₂ photoreduction into CO, Chem. Eng. J. 438 (2022), https://doi.org/10.1016/j.cej.2022.135652.

[51] Y. Shao, X. Wang, Z. Dou, X. Liang, X. Zhang, M. Pang, Q. Xu, M. Ji, M. Wang, Preparation of a ZnIn2S4–ZnAlOx nanocomposite for photoreduction of CO2 to CO, Catal. Sci. Technol. 11 (2021) 3422–3427, https://doi.org/10.1039/D1CY00278C.

[52] L.-Y. Ai, Q. Wang, X.-W. Chen, G.-F. Jiang, Cheap transition metal reinforced donor–acceptor covalent organic frameworks for CO₂ photoreduction, Chem. Eng. J. 475 (2023) 146106, https://doi.org/10.1016/j.cej.2023.146106.